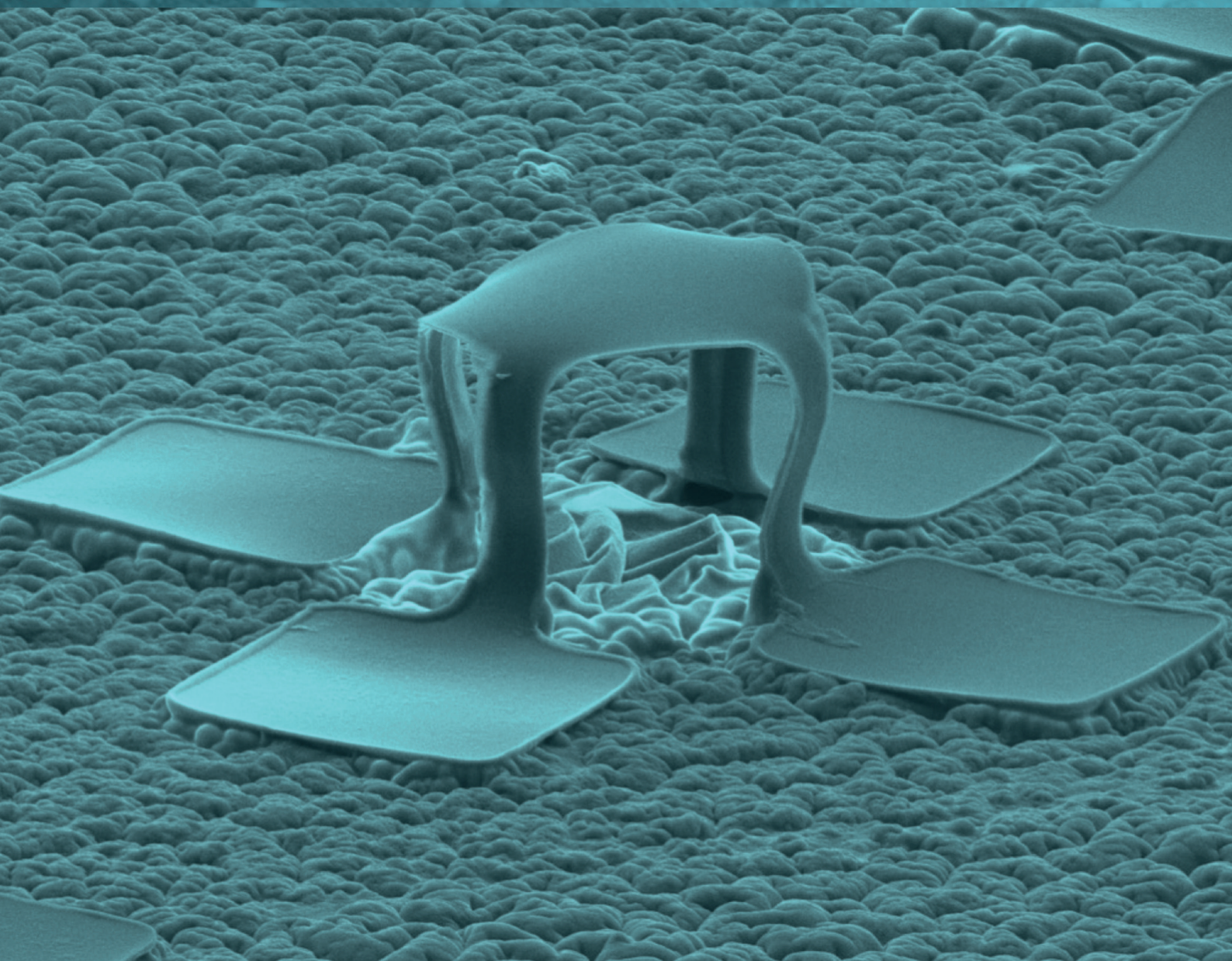


Vol. 14 • No. 11 • March 15 • 2018

[www.small-journal.com](http://www.small-journal.com)

**NANO • MICRO**  
**small**



WILEY-VCH

# Fabrication and Deformation of 3D Multilayered Kirigami Microstructures

Mohammad Humood, Yan Shi, Mengdi Han, Joseph Lefebvre, Zheng Yan, Matt Pharr, Yihui Zhang, Yonggang Huang, John A. Rogers, and Andreas A. Polycarpou\*

Mechanically guided 3D microassembly with controlled compressive buckling represents a promising emerging route to 3D mesostructures in a broad range of advanced materials, including single-crystalline silicon (Si), of direct relevance to microelectronic devices. During practical applications, the assembled 3D mesostructures and microdevices usually undergo external mechanical loading such as out-of-plane compression, which can induce damage in or failure of the structures/devices. Here, the mechanical responses of a few mechanically assembled 3D kirigami mesostructures under flat-punch compression are studied through combined experiment and finite element analyses. These 3D kirigami mesostructures consisting of a bilayer of Si and SU-8 epoxy are formed through integration of patterned 2D precursors with a prestretched elastomeric substrate at predefined bonding sites to allow controlled buckling that transforms them into desired 3D configurations. In situ scanning electron microscopy measurement enables detailed studies of the mechanical behavior of these structures. Analysis of the load–displacement curves allows the measurement of the effective stiffness and elastic recovery of various 3D structures. The compression experiments indicate distinct regimes in the compressive force/displacement curves and reveals different geometry-dependent deformation for the structures. Complementary computational modeling supports the experimental findings and further explains the geometry-dependent deformation.

Biology is inherently based on 3D designs, optimized for performance through billions of years of survival in challenging environments.<sup>[1]</sup> These biological structures span length scales from the nanoscale level, such as DNA,<sup>[2]</sup> to the macroscale, such as shark skin.<sup>[3]</sup> Additionally, these 3D structures often consist of various levels of hierarchy, as exemplified in geckos' feet.<sup>[4]</sup> If the advantages of these fascinating 3D structures can be realized in man-made devices, tremendous advances in capabilities of material systems and architectures will occur, overcoming the inherent limitations of 2D microsystems. For example, 3D microelectromechanical systems (MEMS) offer vastly improved bandwidth and frequency tunability over conventional 2D MEMS structures, such as cantilevered beams and doubly clamped bridges.<sup>[5]</sup>

Indeed, various shapes and scales of 3D structures have been successfully implemented in a number of applications such as wearable electronics,<sup>[6]</sup> robotics,<sup>[7]</sup> solar

M. Humood, Dr. M. Pharr, Prof. A. A. Polycarpou  
Department of Mechanical Engineering  
College of Engineering  
Texas A&M University  
College Station, TX 77843-3123, USA  
E-mail: apolycarpou@tamu.edu

Dr. Y. Shi  
State Key Laboratory of Mechanics and Control of Mechanical Structures  
Nanjing University of Aeronautics and Astronautics  
Nanjing 210016, P. R. China

Dr. Y. Shi, Prof. Y. Zhang  
Center for Mechanics and Materials and Center  
for Flexible Electronics Technology  
AML

Department of Engineering Mechanics  
Tsinghua University  
Beijing 100084, P. R. China

Dr. M. Han, Prof. J. A. Rogers  
Department of Materials Science and Engineering  
Fredrick Seitz Materials Research Laboratory  
University of Illinois at Urbana-Champaign  
Urbana, IL 61801, USA

J. Lefebvre  
Bruker Nano Surfaces  
Eden Prairie, MN 55344, USA

Dr. Z. Yan  
Department of Chemical Engineering and Department of Mechanical  
and Aerospace Engineering  
University of Missouri  
Columbia, MI 65211, USA

Prof. Y. Huang  
Departments of Mechanical Engineering and Civil  
and Environmental Engineering  
Northwestern University  
Evanston, IL 60208, USA

Prof. J. A. Rogers  
Department of Biomedical Engineering, Department of Chemistry,  
Department of Mechanical Engineering,  
Department of Electrical Engineering,  
and Department of Computer Science  
Center for Bio-Integrated Electronics  
Simpson Querrey Institute for Nano/Biotechnology  
Northwestern University  
Evanston, IL 60208, USA

 The ORCID identification number(s) for the author(s) of this article can be found under <https://doi.org/10.1002/sml.201703852>.

DOI: 10.1002/sml.201703852

systems,<sup>[8]</sup> energy storages,<sup>[9]</sup> optoelectronics,<sup>[10]</sup> optomechanical devices,<sup>[11]</sup> and near-field communication (NFC) devices.<sup>[12]</sup> The incorporation of 3D structures has improved performance and extended capabilities in these applications. Different fabrication techniques have been developed to form various 3D structures, including 3D printing,<sup>[13]</sup> two photon/multiphoton lithography,<sup>[14]</sup> and self-assembly.<sup>[15]</sup> However, these methods cannot produce inorganic semiconductors such as silicon.<sup>[16]</sup> Alternatively, mechanically driven assemblies such as strain-induced bending or folding and compressive buckling have the potential to extend the range of materials, including silicon.<sup>[17]</sup> Of these options, compressive buckling offers advantages compared to strain-induced deformation in terms of possible 3D geometries.<sup>[18]</sup> Indeed, in the literature one can find a few hundred different 3D mesostructures with different combinations of materials (polymers, metals, and semiconductors). These structures scale from the sub-micrometer to centimeter scale, thus revealing the scalability of the process.<sup>[19,20]</sup>

The compressive buckling process begins with planar microfabrication of various 2D precursor patterns, consisting of multilayer thin membranes. Next, lithography defines a set of chemically active bonding sites, while reactive ion etching produces patterned cuts in the membrane. Such structures are known as kirigami as their fabrication concept is based on the Japanese art of paper folding and cuts. Transfer printing enables integration of these structures with a prestretched elastomeric substrate.<sup>[21]</sup> Although a variety of 3D mesostructures have been fabricated previously using mechanically guided assembly, their mechanical response to applied loads is still unknown. Thus, in this work we use in situ compression inside the scanning electron microscope (SEM) to investigate their deformation behavior.

The in situ SEM flat punch compression provides capabilities to simultaneously measure load versus displacement and observe deformation in real time.<sup>[22,23]</sup> Thus, this technique can uncover detailed information on material behavior during both compression and postcompression. Numerous 3D structures have been studied using in situ compression, including individual and arrays/foams of carbon nanotubes,<sup>[24]</sup> metals,<sup>[25]</sup> and hierarchical structures of ceramics/polymers.<sup>[26]</sup> However, no reports exist in the literature on the compression of origami- or kirigami-inspired structures.

Herein, we report on the compression of kirigami-inspired structures, which consist of a bilayer of Si and SU-8 (thickness = 200 and 2000 nm, respectively). SU-8 is an epoxy-based photoresist, which is a material commonly used in microfabrication capable of yielding a high aspect ratio even in thick coatings. The SU-8 can be deposited using simple spin-casting and has favorable mechanical properties.<sup>[27]</sup> During in situ compression testing of these kirigami structures, the geometry was found to play a critical role in their flexibility and stretchability. Indeed, we found that structural design enables intrinsically stiff and brittle bulk materials such as Si and SU-8 ( $\approx 2$ – $3$  and  $10$ – $12\%$  tensile strain to fracture, respectively) to undergo large deformation.<sup>[28]</sup> This results in an overall deformable and compliant structure, which can sustain large-scale deformation, including twisting and bending. In light of these experimental findings, a finite element analysis (FEA) model was developed to provide further insight into the maximum stress/strain of kirigami structures during compression.

**Figure 1** illustrates the 2D design patterns and the transformation into 3D structures using compressive buckling. Four different kirigami structures were made using a fixed prestrain of 65%. The red color represents the bonding region to the elastomer substrate. Silicone was used as a platform for the assembly of these structures. SEM images were taken before the start of the in situ compression experiments (see Figure 1b). A  $12\ \mu\text{m}$  diameter fiber is seen in front of the table structure and provides a perception about the size of these structures.

Precise height measurements for the four fabricated structures were taken using a profilometer. The height was found to be  $75\ \mu\text{m}$  for the table and ring structures and  $70\ \mu\text{m}$  for the tent and rotated table structures. For the rotated table, due to the inclined top surface, the height was averaged. The in situ compression was carried out in two steps. In this study, we defined the percentage of compression based on the height measurement for each structure. For example, 50% compression refers to  $35\ \mu\text{m}$  of vertical displacement of the flat punch, while  $70\ \mu\text{m}$  displacement represents 100% compression of the rotated table structure. All structures, except the tent, were compressed to  $\approx 50\%$  of their initial height followed by a complete unloading of the flat-punch. 5 min was set as a wait time to allow relaxation of the structure and substrate before carrying out the next experiment of 100% compression. Both the 50 and 100% compression experiments were performed on the same structure except for the tent structure. These two experiments were repeated on a second sample for each structure to assess repeatability. The first tent was compressed to 30% while the second tent was compressed to 100%.

**Figure 2** shows typical load–displacement curves for the four structures. The recorded videos for the compression experiments are provided in Movies S1–S8 (Supporting Information). The load–displacement curves demonstrated three regions in the compression of kirigami structures: linear deformation, rapid buckling, and stiffening behavior. The three regions are marked in Figure 2a and are similar to those identified in other 3D structures, such as foam-like arrays of carbon nanotubes.<sup>[29]</sup> The deformation was linear and nearly recoverable from the point of contact to 50% compression. For the second region, the reduction in the slope of the load–displacement plot indicates rapid buckling, that is, large displacements produce small increases in force. Once approaching a compression of 100%, the stiffness increased due to the nonlinear compression of the legs of the structures accompanied by deformation of the substrate.

Similarly, unloading the structures showed the substrate effect. All structures showed the unloading curve with two different slopes, except the tent structure. The change in the slope took place around  $50\ \mu\text{m}$  displacement. This indicated two distinct unloading behaviors after removal of the flat punch. First, the substrate recovered quickly followed by a mixed relaxation of both the structure and the substrate. Indeed, this could be seen in Movies S1–S3 (Supporting Information). The tent structure showed a drop in the load at  $\approx 100\%$  compression, which correlated with a twisting of the structure in the recorded video (Movie S4, Supporting Information).

The load–displacement curves highlight different levels of energy dissipation for each kirigami structure based on the area under the load–displacement curve. The rotated table structure

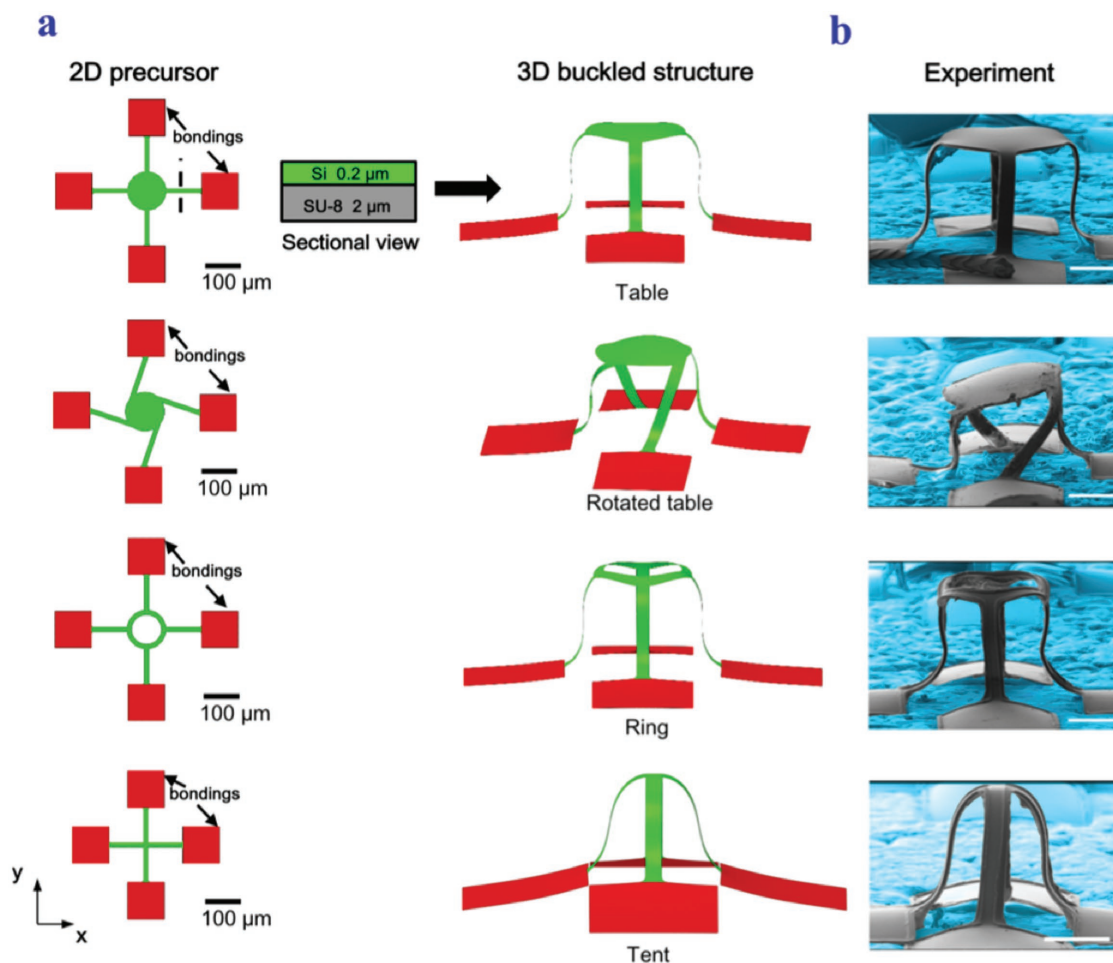


**Figure 1.** a) Conceptual illustration of the 3D kirigami structures, which were assembled from 2D precursors by compressive buckling using FEA results (scale bar is 100 μm); b) Corresponding SEM images for the 3D structures (scale bar is 30 μm).

had the lowest energy dissipation, followed by the ring, and finally the table and the tent structures. The elastic recovery followed the same order, that is, the rotated table structures showed the highest elastic recovery. The energy dissipation is due to viscoelastic/plastic effects and possible fracture events. Therefore, structures with lower energy dissipation exhibited higher elastic recovery. **Table 1** shows the response to mechanical compression for all the structures as a function of the load carrying capability, elastic recovery, and unloading stiffness. Both the maximum load and stiffness were calculated using 50% compression experiments to avoid substrate effects. The elastic recovery was calculated using the 100% compression experiments. A correlation exists between the stiffness and recoverability, where a stiffer structure exhibits less elastic recovery.

**Figure 3** provides further insight into the deformation of each structure by taking snapshots from each movie during compression. The snapshots were taken at intervals of 0, 25, 50, and 100% compression. The structures experienced either onefold bending, twofold bending, or bending and twisting. The deformation in the table structure took place both inward (toward SU-8) and outward (towards Si), as illustrated by the arrows in Figure 3. That is, some regions of the Si thin film experienced tension while others experienced compression.

These images help explain the rapid buckling or softening of the table structure, as they undergo larger elongation in the legs in the form of twofold bending. Due to the rotated arrangement of the legs, the rotated table structure deformed by both bending and twisting. Finally, both the ring and tent structures experienced onefold bending. Additionally, the tent structure exhibited slight twisting upon reaching close to 100% compression. The arrows in Figure 3 provide an illustration of the deformation direction. For example, the double arrows for the table structure show twofold bending.

Corresponding FEA simulations were carried out using the commercial software (ABAQUS) and the distributions of maximum principal strain in the Si layer under different stages of compression are also shown in Figure 3. Good agreement of the deformation patterns can be observed between FEA and experiments, for all of the cases studied in this work. The FEA results indicate strain concentrations at the ribbon–membrane connection regions in the table and rotated-table structures, as well as the ribbon–ribbon connection regions in the ring and tent structures. This is in accordance with the relatively small radius of curvature at these regions. FEA predicts slight twisting of the tent structures once reaching 100% compression, in agreement with the experiments.

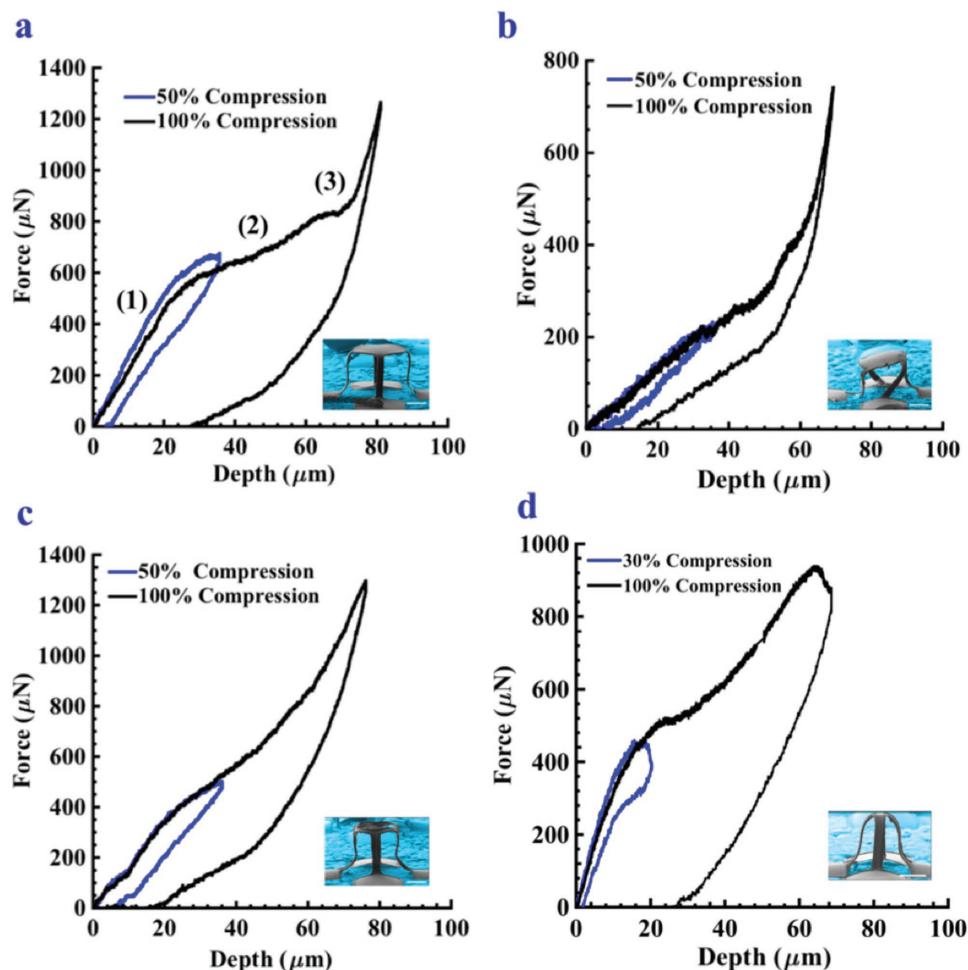


**Figure 2.** Load versus displacement data for flat-punch compression of a) table, b) rotated table, c) ring, and d) tent structures.

While Figure 3 provides in situ snapshots from the recorded experimental and FEA movies, **Figure 4** shows the SEM images at higher resolution, taken before and after each experiment. The 50% compression experiments were nearly recoverable, and there was no change in the shape of the legs. However, the 100% compression experiments yielded observable plastic deformation in all structures except the rotated table structure, which recovered to the initial height. The three other structures had similar residual deformation in the legs in the form of sharp curvature toward the SU-8 layer. Even though the table structure had twofold bending, the bottom bending toward the

**Table 1.** Comparison between kirigami structures in terms of response to mechanical deformation.

Structure	Maximum load bearing <sup>a)</sup> [μN]	Max compression depth <sup>a)</sup> [μm]	Elastic recovery [%]	Unloading stiffness <sup>a)</sup> [N m <sup>-1</sup> ]
Rotated table	220	36.1	89.5	6.1
Ring	500	36.2	84.2	13.9
Table	670	35.6	77.7	18.1
Tent	450	20.4	70.2	23.7

<sup>a)</sup> Properties measured at 50% compression experiments to avoid substrate effects.

SU-8 layer was larger and left larger residual curvature likely revealing possible plastic deformation or fracture in the SU-8 layer. If the SU-8 film yielded and the maximum strain was higher than the fracture threshold of SU-8 ( $\approx 10\text{--}12\%$ ),<sup>[30]</sup> the SU-8 will not recover fully and elastically. If SU-8 experiences elastic behavior before this threshold, then it will break without a plastic domain.<sup>[31]</sup> Fracture events might explain the softening (rapid buckling) for the structures above 50% compression. Since the thickness of the Si layer is 10% of the SU-8 layer, fracture events are expected to be experienced by the thicker SU-8 epoxy layer first.

To better understand the residual curvatures in the legs of the structures, FEA was carried out to calculate the von Mises stress and maximum principal strains. The von Mises stress is used to predict the yielding of a material once subjected to a complex loading, while the maximum principal strain provides the largest normal strain, which is of interest to understand the deformation and/or fracture in the SU-8 layer under compression. Similar contours are provided in the Supporting Information for the Si layer under compression.

**Figure 5b** revealed insights about the maximum strain experienced by the structures under 100% compression. Only the rotated table structure had a maximum principal strain ( $\approx 8.0\%$ )

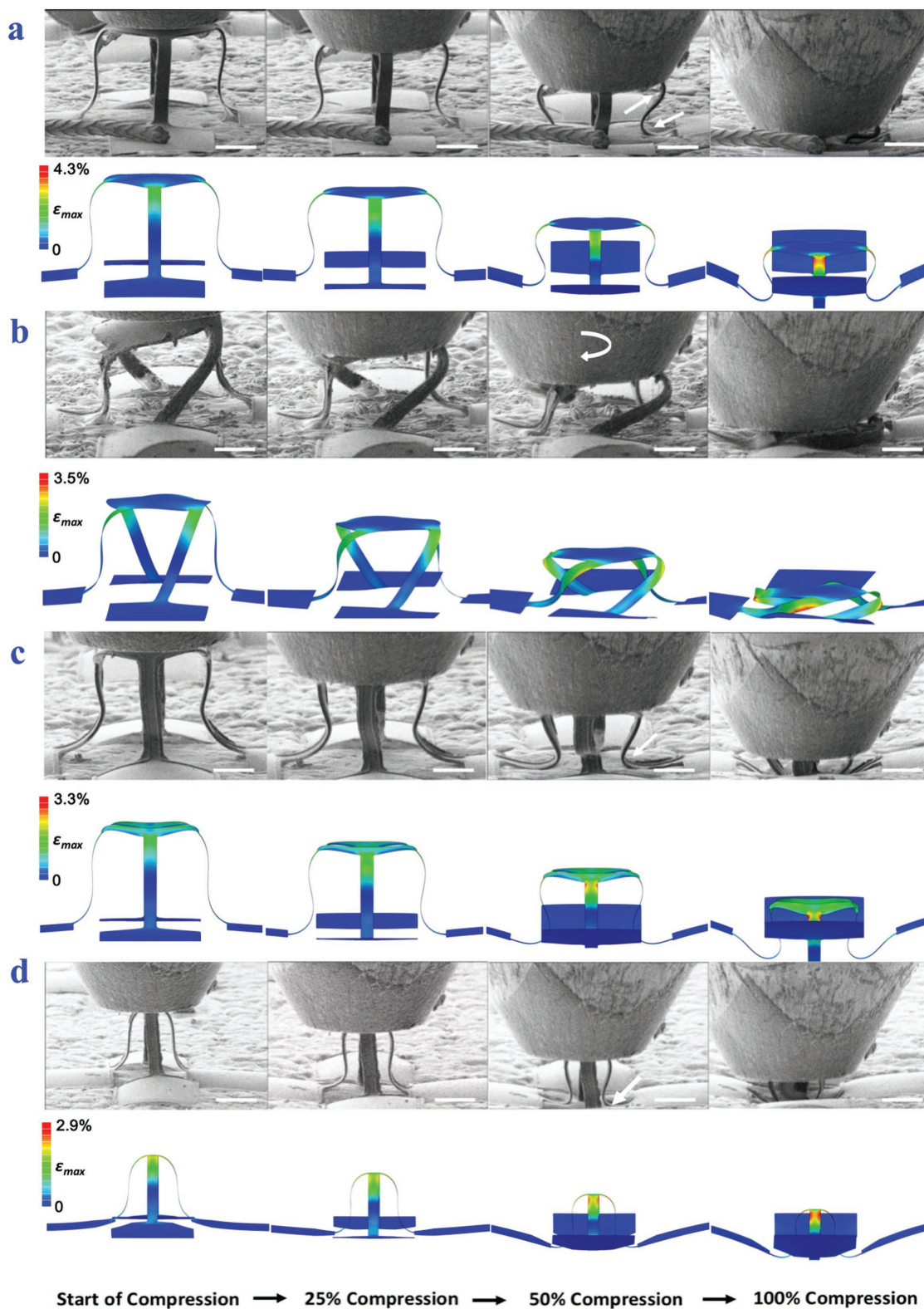


**Figure 3.** Snapshots taken from the recorded movies (experiments and FEA) at the start of the compression, 25, 50, and 100% compression for the a) table, b) rotated table, c) ring, and d) tent structures (scale bar is 30  $\mu\text{m}$ ).

lower than 10%, therefore it maintained an elastic deformation. Other structures experienced strains higher than the fracture

strain threshold of SU-8, which led to the residual change in the curvature of the legs and potentially fracture events. In

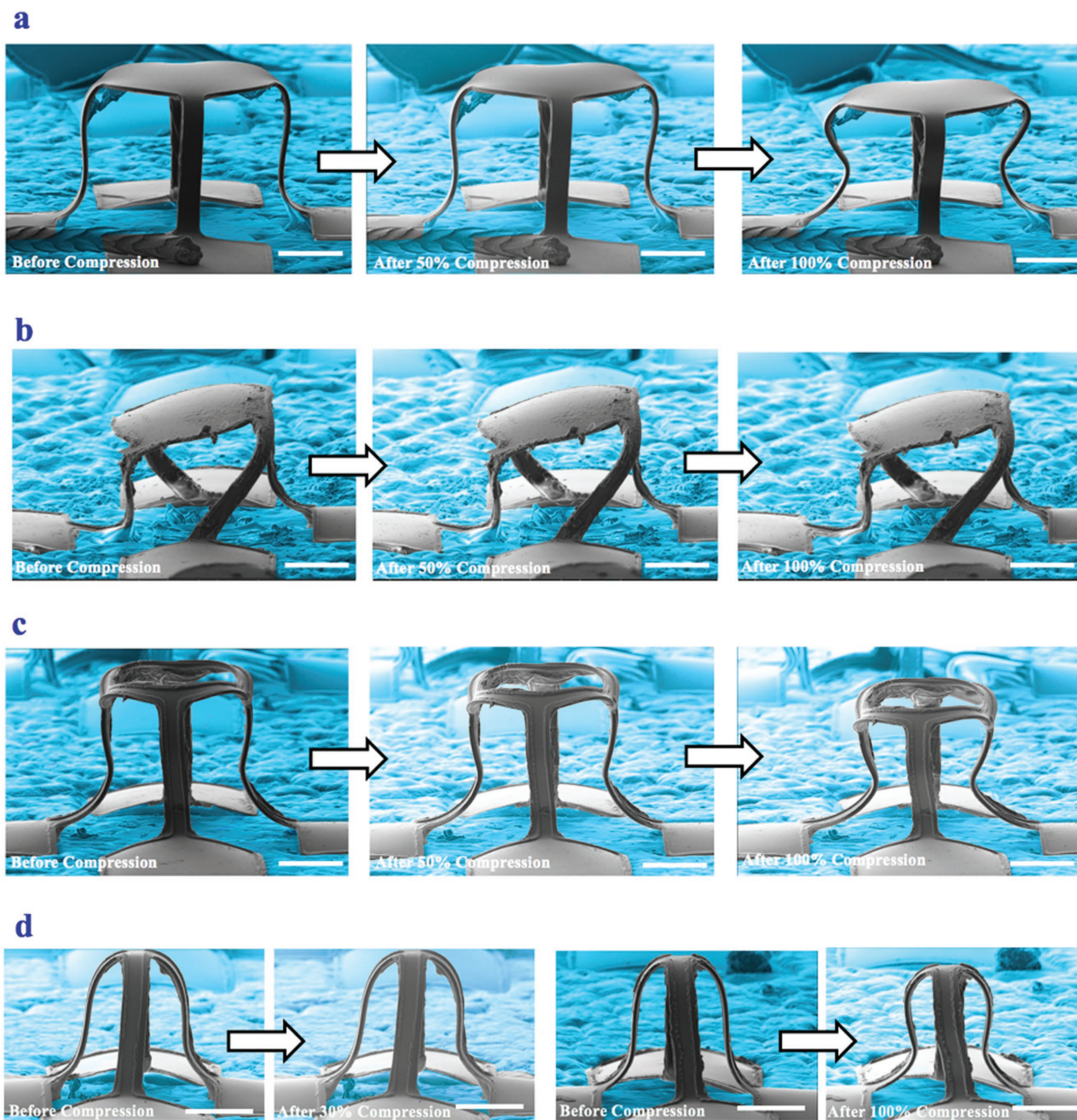


**Figure 4.** SEM images taken before the start of compression, after 30–50%, and after 100% compression for the a) table, b) rotated table, c) ring, and d) tent (scale bar is 30  $\mu\text{m}$ ).

terms of stress, structures with bending-dominated deformation experienced high stresses in the bottom of the legs. On the other hand, the rotated table structure had higher stresses in the top part of the legs due to the combined bending/twisting deformations.

Figure S1 (Supporting Information) shows contours of von Mises stress and maximum principal strain in the Si layer only for all the fully compressed structures. The maximum strain (stress) is mainly located at the ribbon–ribbon (or ribbon–membrane) connections, which means the compression loading is mainly taken by these regions. The maximum

principal strain for the Si layer is about 4.3% for the table structure, and in the range of 2.9–3.5% for the other structures. Even though the maximum strain is slightly higher than the maximum tensile strain to fracture for bulk Si (2–3%), other researchers reported that nanoscale silicon structures can reach higher tensile strains of  $\approx$ 5–7% without fracture.<sup>[32]</sup> Indeed, yielding does not occur in single-crystalline silicon until fracture takes place. The yield strength is 7000 MPa,<sup>[33]</sup> and only the table structure approached this limit. Therefore, there is no indication of fracture or crack in the silicon layer. We anticipate that fracture could have

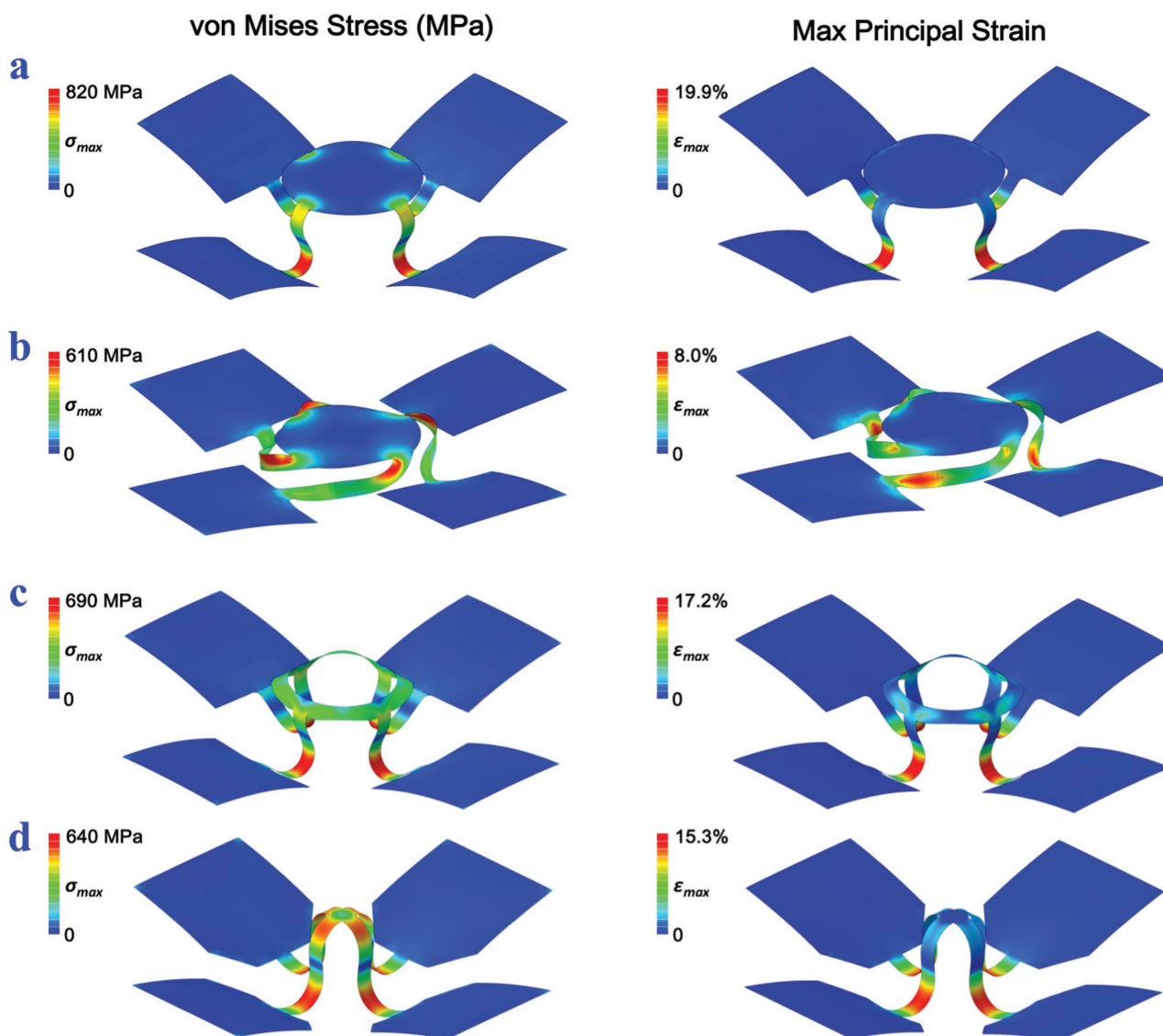


**Figure 5.** FEA results for the compression of SU-8 layer in the kirigami structures (under 100% compression) showing von Mises stress (MPa, left column) and maximum principal strain (right column) for the a) table, b) rotated table, c) ring, and d) tent. The substrate and punch were removed to allow visual observation of the stress and strain contours in the structures.

occurred in the thicker SU-8 layer for the table, ring, and tent structures, where the strain was higher than the fracture threshold of SU8 ( $\approx 10\%$ ).

This work discussed the fabrication and deformation of 3D Si/SU-8 kirigami structures, which have potential applications in 3D NFC devices and 3D MEMS devices. The operation of these devices requires a high level of mechanical reliability of their components. For example, MEMS are made of silicon and its oxides, which are inherently stiff and brittle, and can undergo only 2–3% tensile strain to fracture in 2D configurations. However, silicon can undergo larger deformations without fracture once fabricated in 3D configurations, as shown herein and by other researchers.

Multilayered 2D precursors of brittle Si and SU-8 buckled to create functional flexible 3D structures. In situ flat punch compression provided insight into the deformation mechanics of

kirigami structures. In particular, during 50% compression, the structures recovered elastically back to their initial heights. By comparison, 100% compression produced permanent changes and possible microfracture events in the curvature of the legs of the structures. Still, no experimental evidence of the microcracks/delamination was observed in the structures, even up to 100% compression, thereby highlighting the flexibility of these structures. Computational FEA modeling supported the experimental findings and provided further insight into the dependence of deformation on the geometry of the structures. The mechanical and geometric properties (such as bending stiffness) at the connections play an important role during the deformation (compression, bending, or twisting) of the structures and influence the final configuration of the kirigami structures, which should be considered during the design of such 3D structures.

In addition, the energy dissipated by these structures is important as it indicates whether they will be durable against repeated deformations and maintain stable hysteretic cycling. Future work needs to focus in addressing how these structures behave under repeated compressive load. The energy dissipation is due to viscoelastic and plastic effects. Therefore, the strain rate and other time-dependent properties need to be explored as well for both the structures and the substrate. Besides geometry and time-dependent properties, the thickness of each of the Si and SU8 layer, which is not studied here, could be a variable to reduce the maximum strain (stress) in the structure. The agreement between the computational and experimental results suggests the possibility for future computational simulations to optimize precursor design for load bearing, energy dissipation, and elastic recovery capabilities.

## Experimental Section

**Materials and Fabrication:** Preparation of 2D precursors of silicon and epoxy (SU8) bilayers exploited photolithography and reactive ion etching to pattern a thin layer of silicon (200 nm in thickness) using silicon on insulator (SOI) wafer. Wet etching by hydrofluoric acid (HF) fully dissolved the exposed silicon dioxide (1  $\mu\text{m}$  in thickness) on the SOI wafer. The following spin-coating and photolithography steps defined the pattern of the epoxy (SU8) layer (2  $\mu\text{m}$  in thickness) on top of the silicon layer. Another spin-coated and lithographically defined photoresist layer (AZ 5214, 4  $\mu\text{m}$  in thickness) covered the silicon and epoxy (SU8) patterns but left the bonding regions exposed. Wet etching in HF fully removed all the silicon dioxide underneath the patterns, thereby facilitating the transfer printing process. Deposition of titanium (5 nm in thickness) and silicon dioxide (50 nm) through electron beam evaporation promoted the adhesion of the bonding regions.

Transfer printing of the 2D precursors began with retrieving the patterns from SOI wafer to a polydimethylsiloxane (PDMS) stamp. Laminating water-soluble tape onto the PDMS surface enabled the transfer of 2D precursors from PDMS stamp to water-soluble tape. The buckling process utilized silicone elastomer (Dragon Skin, 600  $\mu\text{m}$  in thickness) as the assembly substrate. Ultraviolet–ozone treatment of the silicone elastomer and 2D precursors on water-soluble tape induced hydroxyl termination for strong bonding. The silicone elastomer was then stretched to carry the 2D precursors along with the water-soluble tape. Heating at 70  $^{\circ}\text{C}$  for 8 min formed strong chemical bonding between the bonding regions of the 2D precursors and silicone elastomer. After dissolving water-soluble tape with water and AZ 5214 as acetone, releasing the prestrain applied to the silicone elastomer enabled out-of-plane translations of the nonbonding regions.

**Mechanical Characterization:** A PI 88 SEM PicoIndenter (Bruker Nano Surfaces, Eden Prairie, MN) was used to perform the in situ compression experiments. An extended range (xR) transducer allowed for large displacement up to 150  $\mu\text{m}$ . The indenter itself consisted of a diamond flat punch with a 100  $\mu\text{m}$  diameter. The experiments utilized a displacement-controlled mode at a loading rate of 1  $\mu\text{m s}^{-1}$ . The samples were coated with 5 nm of Pt/Pd to provide charge dissipation during SEM observation.

**Finite Element Analysis:** 3D FEA simulated the final configurations and strain distributions of the 3D structures using the commercial software ABAQUS. The kirigami structures consisted of four-node shell elements, and the elastomer substrates consisted of eight-node 3D stress elements. Surface contact is applied between the structure and substrate with friction coefficient of 0.3 (“penalty” setting for tangential behavior and “hard contact” for normal behavior in ABAQUS). Convergence of mesh sizes ensured computational accuracy. The elastomer substrate was modeled using a hyperelastic constitutive relation (Mooney–Rivlin model) with parameters  $C_{10} = 0.06757$  MPa,  $C_{01} = 0.01689$  MPa, and

$D_1 = 0.48$  MPa $^{-1}$  in ABAQUS. The elastic moduli ( $E$ ) and Poisson’s ratios ( $\nu$ ) for SU-8 and silicon were  $E_{\text{SU-8}} = 4.02$  GPa,  $\nu_{\text{SU-8}} = 0.22$ ,  $E_{\text{Si}} = 130$  GPa, and  $\nu_{\text{Si}} = 0.27$ .

## Supporting Information

Supporting Information is available from the Wiley Online Library or from the authors.

## Acknowledgements

Funding of this study was provided from the Hagler Institute for Advanced Study (HIAS) at Texas A&M University. Y.Z. acknowledges the support from the National Natural Science Foundation of China (Grant Nos. 11672152 and 11722217) and the Tsinghua National Laboratory for Information Science and Technology.

## Conflict of Interest

The authors declare no conflict of interest.

## Keywords

3D mesostructures, damage tolerance, in situ compression, kirigami, recovery

Received: November 5, 2017

Revised: December 2, 2017

Published online: January 29, 2018

- [1] U. G. K. Wegst, H. Bai, E. Saiz, A. P. Tomsia, R. O. Ritchie, *Nat. Mater.* **2015**, *14*, 23.
- [2] F. Zhang, F. Hong, H. Yan, *Nat. Nanotechnol.* **2017**, *12*, 189.
- [3] L. Wen, J. C. Weaver, G. V. Lauder, *J. Exp. Biol.* **2014**, *217*, 1656 LP.
- [4] C. Zhang, D. A. Mcadams, J. C. Grunlan, *Adv. Mater.* **2016**, *28*, 6292.
- [5] X. Ning, H. Wang, X. Yu, J. A. N. T. Soares, Z. Yan, K. Nan, G. Velarde, Y. Xue, R. Sun, Q. Dong, H. Luan, C. M. Lee, A. Chempakasseril, M. Han, Y. Wang, L. Li, Y. Huang, Y. Zhang, J. A. Rogers, *Adv. Funct. Mater.* **2017**, *27*, 1605914.
- [6] Y. Su, X. Ping, K. J. Yu, J. W. Lee, J. A. Fan, B. Wang, M. Li, R. Li, D. V. Harburg, Y. Huang, C. Yu, S. Mao, J. Shim, Q. Yang, P.-Y. Lee, A. Armonas, K.-J. Choi, Y. Yang, U. Paik, T. Chang, T. J. Dawidczyk, Y. Huang, S. Wang, J. A. Rogers, *Adv. Mater.* **2017**, *29*, 1604989.
- [7] J. C. Breger, C. Yoon, R. Xiao, H. R. Kwag, M. O. Wang, J. P. Fisher, T. D. Nguyen, D. H. Gracias, *ACS Appl. Mater. Interfaces* **2015**, *7*, 3398.
- [8] A. Lamoureux, K. Lee, M. Shlian, S. R. Forrest, M. Shtein, *Nat. Commun.* **2015**, *6*, 8092.
- [9] Z. Song, T. Ma, R. Tang, Q. Cheng, X. Wang, D. Krishnaraju, R. Panat, C. K. Chan, H. Yu, H. Jiang, *Nat. Commun.* **2014**, *5*, 3140.
- [10] J. Kim, G. A. Salvatore, H. Araki, A. M. Chiarelli, Z. Xie, A. Banks, X. Sheng, Y. Liu, J. W. Lee, K.-I. Jang, S. Y. Heo, K. Cho, H. Luo, B. Zimmerman, J. Kim, L. Yan, X. Feng, S. Xu, M. Fabiani, G. Gratton, Y. Huang, U. Paik, J. A. Rogers, *Sci. Adv.* **2016**, *2*, 1600418.
- [11] Y. Tang, G. Lin, S. Yang, Y. K. Yi, R. D. Kamien, J. Yin, *Adv. Mater.* **2017**, *29*, 1604262.

- [12] Z. Yan, F. Zhang, F. Liu, M. Han, D. Ou, Y. Liu, Q. Lin, X. Guo, H. Fu, Z. Xie, M. Gao, Y. Huang, J. Kim, Y. Qiu, K. Nan, J. Kim, P. Gutruf, H. Luo, A. Zhao, K.-C. Hwang, Y. Huang, Y. Zhang, J. A. Rogers, *Sci. Adv.* **2016**, 2, 1601014.
- [13] D. Lin, Q. Nian, B. Deng, S. Jin, Y. Hu, W. Wang, G. J. Cheng, *ACS Nano* **2014**, 8, 9710.
- [14] D. W. Yee, M. D. Schulz, R. H. Grubbs, J. R. Greer, *Adv. Mater.* **2017**, 29, 1605293.
- [15] R. M. Zadegan, M. D. E. Jepsen, K. E. Thomsen, A. H. Okholm, D. H. Schaffert, E. S. Andersen, V. Birkedal, J. Kjems, *ACS Nano* **2012**, 6, 10050.
- [16] S. H. Kang, M. D. Dickey, *MRS Bull.* **2016**, 41, 93.
- [17] S. Xu, Z. Yan, K.-I. Jang, W. Huang, H. Fu, J. Kim, Z. Wei, M. Flavin, J. McCracken, R. Wang, A. Badea, Y. Liu, D. Xiao, G. Zhou, J. Lee, H. U. Chung, H. Cheng, W. Ren, A. Banks, X. Li, U. Paik, R. G. Nuzzo, Y. Huang, Y. Zhang, J. A. Rogers, *Science* **2015**, 347, 154.
- [18] Y. Shi, F. Zhang, K. Nan, X. Wang, J. Wang, Y. Zhang, Y. Zhang, H. Luan, K.-C. Hwang, Y. Huang, J. A. Rogers, Y. Zhang, *Extreme Mech. Lett.* **2017**, 11, 105.
- [19] Y. Zhang, F. Zhang, Z. Yan, Q. Ma, X. Li, Y. Huang, J. A. Rogers, *Nat. Rev. Mater.* **2017**, 2, 17019.
- [20] Z. Yan, M. Han, Y. Yang, K. Nan, H. Luan, Y. Luo, Y. Zhang, Y. Huang, J. A. Rogers, *Extreme Mech. Lett.* **2017**, 11, 96.
- [21] S. Kim, J. Wu, A. Carlson, S. H. Jin, A. Kovalsky, P. Glass, Z. Liu, N. Ahmed, S. L. Elgan, W. Chen, P. M. Ferreira, M. Sitti, Y. Huang, J. A. Rogers, *Proc. Natl. Acad. Sci. USA* **2010**, 107, 17095.
- [22] S. B. Hutchens, L. J. Hall, J. R. Greer, *Adv. Funct. Mater.* **2010**, 20, 2338.
- [23] R. M. Delaine-Smith, S. Burney, F. R. Balkwill, M. M. Knight, *J. Mech. Behav. Biomed. Mater.* **2016**, 60, 401.
- [24] S. Ozden, Y. Yang, C. S. Tiwary, S. Bhowmick, S. Asif, E. S. Penev, B. I. Yakobson, P. M. Ajayan, *Nano Lett.* **2016**, 16, 232.
- [25] L.-Y. Chen, J.-Q. Xu, H. Choi, M. Pozuelo, X. Ma, S. Bhowmick, J.-M. Yang, S. Mathaudhu, X.-C. Li, *Nature* **2015**, 528, 539.
- [26] L. R. Meza, A. J. Zelhofer, N. Clarke, A. J. Mateos, D. M. Kochmann, J. R. Greer, *Proc. Natl. Acad. Sci. USA* **2015**, 112, 11502.
- [27] H. Lorenz, M. Despont, N. Fahrni, J. Brugger, P. Vettiger, P. Renaud, *Sens. Actuators, A* **1998**, 64, 33.
- [28] A. Das, A. Sinha, V. R. Rao, K. N. Jonnalagadda, *Exp. Mech.* **2017**, 57, 687.
- [29] M. R. Maschmann, Q. Zhang, R. Wheeler, F. Du, L. Dai, J. Baur, *ACS Appl. Mater. Interfaces* **2011**, 3, 648.
- [30] T. Xu, J. H. Yoo, S. Babu, S. Roy, J.-B. Lee, H. Lu, *J. Microelectromech. Syst.* **2016**, 26, 105001.
- [31] F. Chollet, SU-8: Thick Photo-Resist for MEMS, <http://memscyclopedia.org/su8.html>, (accessed Sept. 2017).
- [32] H. Zhang, J. Tersoff, S. Xu, H. Chen, Q. Zhang, K. Zhang, Y. Yang, C.-S. Lee, K.-N. Tu, J. Li, Y. Lu, *Sci. Adv.* **2016**, 2, 1501382.
- [33] K. E. Petersen, *Proc. IEEE* **1982**, 70, 420.